

Point-Pattern Matching Technique for Local Structural Analysis in Condensed Matter

Arash Dehghan Banadaki¹, Jason J. Maldonis², Paul M. Voyles², and Srikanth Patala^{1,*}

¹Department of Materials Science and Engineering, North Carolina State University, Raleigh, NC

²Department of Materials Science and Engineering, University of Wisconsin-Madison, Madison, WI

*spatala@ncsu.edu

ABSTRACT

The local arrangement of atoms is one of the most important predictors of mechanical and functional properties of materials. However, algorithms for identifying the geometrical arrangements of atoms in complex materials systems are lacking. To address this challenge, we present a point-pattern matching algorithm that can detect instances of a “template” structure in a given set of atom coordinates. To our knowledge this is the first geometrical comparison technique for atomistic configurations with very different number of atoms, and when the optimal rotations and translations required to align the configurations are unknown. The pattern matching algorithm can be combined with an appropriate set of metrics to quantify the similarity or dissimilarity between configurations of atoms. We demonstrate the unique capabilities of the point-pattern matching algorithm using two examples where the automated analysis of local atomistic structure can help advance the understanding of structure-property relationships in material science: (a) identifying local three-dimensional polyhedral units along interfacial defects, and (b) the analysis of quasi-icosahedral topologies in the atomistic structure of metallic glasses. We anticipate that the pattern matching algorithm will be applicable in the analysis of atomistic structures in broad areas of condensed matter systems, including biological molecules, polymers and disordered metallic systems. An online implementation of the algorithm is provided via the open source code hosted on GitHub (<https://github.com/spatala/ppm3d>).

1 Introduction

In materials science, structure is typically described using atoms as fundamental units and the properties are inferred through the spatial arrangements of atoms relative to each other. The length scales involved may vary from short-range (near-neighbors) and medium-range to long-range depending on the structure and properties of interest. Even when the analysis of structure at larger length scales is necessary, the characterization of the relative arrangement of atoms in the first coordination shell has proven to be of great importance^{1,2}. For perfect crystals, the machinery of crystallography provides a complete, succinct, and extremely powerful description of the positions of all the atoms, but there is no parallel description for aperiodic structures, including defects in crystalline materials such as grain boundaries and the structure of glasses. In such cases, we do not have a general description (or quantification) of even the local structure. A parallel problem arises in atomistic simulations. In this case, the position of every atom is known, often as a function of time, yielding a great deal of data, but leaving us with a need for a general, automated analysis approach to develop abstract structural descriptions from this detailed data.

Some of the most commonly utilized structural analysis methods for atomistic simulations include: centro-symmetry parameter, bond-order analysis, common-neighbor analysis, bond angle analysis, and Voronoi-cell topology. The first four techniques involve computing for each atom in the system a scalar quantity, an order-parameter, which depends on the spatial location of the atom's neighbors. Voronoi-cell topology uses a topological descriptor, the Voronoi index or the p -vector^{3,4}, instead of a scalar calculated from spatial locations as the order parameter. These quantities are invariant to rigid body rotations and translations of the local atomic environment. While these simplified order parameters have been invaluable in the analysis of the distributions of different types of defects and their evolution during atomistic simulations, they suffer from issues involved with degeneracies and large sensitivity to small perturbations. The degeneracies arise as the order parameters are simply projections of a high-dimensional atomistic configuration space to a single scalar value, as described in Lazar *et al.*² For example, the centro-symmetry parameter exhibits similar values for either an atom that is present along a defect (such as a dislocation or a grain boundary) or one that is in a bulk single crystal at moderately high temperatures (*e.g.* $0.5 T_m$).

The issue of high sensitivity to small perturbations is evident when using the Voronoi cell topology as a descriptor. For any topological descriptor, there will exist atomic configurations where a small change in the position of one of the atoms will change the topology of the descriptor. Lazar *et al.*² introduced the theory of λ -types for Voronoi topologies in an attempt to quantify the effect of perturbations. In simple terms, all the distinct Voronoi topologies that are obtained by small perturbations of the center atom and its neighbors are grouped together as belonging to one family of Voronoi polyhedra. Different families correspond to distinct arrangements of local atomic structure. While this classification has proven successful in distinguishing atomic structures in crystal lattices from those along defects (even with thermal vibrations), two aspects of the algorithm limit its applicability: (a) the different types of possible perturbations have to be enumerated in order to identify the family of each Voronoi polyhedron, and (b) degeneracies will arise as a unique Voronoi topology may be obtained through a perturbation of two distinct Voronoi polyhedra. These limitations are particularly troublesome for disordered materials, such as metallic glasses. As shown in Figure 2 in Ref 1, the diversity of the type of clusters that may be present in glasses is large and hence an enumeration method is not practical. As such, any topological description will suffer from the difficulty of degeneracy.

Another common limiting feature of the structure classifiers is that all the quantities measured are per-atom quantities. That is, each atom gets a scalar value or a topological index. However, in complex systems *e.g.* along defects such as dislocations and grain boundaries⁵ or in quantifying medium-range order in glasses, it is the geometrical patterns and the connectivity of a sub-set of atoms in the system that are of interest. None of the techniques described above are able to discern the patterns generated by atomic arrangements in material systems.

In order to overcome these challenges, we propose a point-pattern matching technique for direct characterization of local atomic structures. Point-pattern matching (PPM) is a fundamental problem in pattern recognition with applications in a broad range of fields including computer vision⁶⁻¹¹, computational chemistry^{12,13}, astronomy^{14,15} and computational biology^{16,17}. More specifically, PPM methods are *feature detection algorithms* that can identify specific features in an environment. PPM techniques use a metric to quantify the similarity (or dissimilarity) between

atomic environments, as described in section 1.1. This allows for a quantitative measure of how structure changes, for example, as temperature is increased or when the crystallographic nature of the defect is varied (see section 2.1). PPM algorithms can also account for small perturbations that arise due to thermal vibrations, making them ideal for the analysis of local atomic structure in disordered material systems. Most notably, with a suitable metric, unsupervised machine learning algorithms, such as clustering, can be used to analyze the underlying geometries in the material¹⁸.

In the following sections, we first introduce the PPM algorithm with a simple two-dimensional example. Then, we present two material science problems illustrating the unique capabilities of the PPM algorithm for analyzing structures in atomistic models. The first is the identification of geometrical motifs in the disordered regions of a metallic grain boundary, and the second identifies icosahedral geometry in a Zr-Cu-Al metallic glass.

1.1 Methodology

In the terminology used in image-processing, atoms are referred to as points and the sets of atoms being compared are point-sets. To quantify the (dis)similarity between two point-sets, we compare a set of m points (the *model*, \mathbf{M} also known as the *template*) to a set of n points (the *target*, \mathbf{T}). The positions of the points in the model, \mathbf{M} , and in the target, \mathbf{T} , are given by the set of vectors $\mathbf{R}^{\mathbf{M}} = \{\mathbf{r}_1^{\mathbf{M}}, \mathbf{r}_2^{\mathbf{M}}, \dots, \mathbf{r}_m^{\mathbf{M}}\}$ and $\mathbf{R}^{\mathbf{T}} = \{\mathbf{r}_1^{\mathbf{T}}, \mathbf{r}_2^{\mathbf{T}}, \dots, \mathbf{r}_n^{\mathbf{T}}\}$, respectively. The objective is to find a set of m points in the target that are most similar to the configuration of points in the model set. That is, we wish to find a one-to-one mapping between the atoms in the model and the target, a rotation matrix, and a translation vector that best overlaps the points in the model with those in the target set.

In the general problem, the number of points n in the target is greater than those in the model, *i.e.* $n \geq m$. A brute-force technique requires picking $\binom{m}{n}$ sub-sets of m points in the target, and finding the correspondence requires another $m!$ comparisons. Hence, the algorithm, in the worst case, has the complexity of $O(n!/(n-m)!)$, which is computationally unfeasible for large values of n and m . A wide variety of approaches have been proposed in the fields of image processing^{19,20} and computational chemistry^{21–30} to render this general problem computationally feasible.

For condensed-matter systems, the goal is to compare and characterize molecular structures, which in general allows us to assume an equal number of atoms in the model and the target (*i.e.* $n = m$). For $n = m$, the similarity (or dissimilarity) between point-sets is quantified using the root-mean-square-distance (RMSD) parameter, defined as²³:

$$\text{RMSD} = \frac{1}{\sqrt{m}} \min_{f, U, \mathbf{t}} \sum_{i=1}^m d\left(U\mathbf{r}_i^{\mathbf{M}} + \mathbf{t}, \mathbf{r}_{f(i)}^{\mathbf{T}}\right), \quad (1)$$

where $d(\cdot, \cdot)$ is the Euclidean distance metric. The minimization is over all possible permutations of indices, given by the function f , rotations of the model, U , and relative translations \mathbf{t} . The permutation function f maps the indices of the points in the model to those in the target. For example, if $f(i^{\mathbf{M}}) = j^{\mathbf{T}}$, then the i^{th} index in the model is mapped to the j^{th} index in the target (the same information may also be represented using a $m \times m$ permutation matrix). We denote the operations f , U and \mathbf{t} that minimize RMSD as \hat{f} , \hat{U} , and $\hat{\mathbf{t}}$, respectively. The RMSD defined as such obeys the three properties of a metric³¹: (a) the coincidence axiom, (b) symmetry, and (c) the triangle inequality.

If the minimizing rotations and translations, \hat{U} , and $\hat{\mathbf{t}}$, are known *a priori*, the permutation matrix can be obtained using the Hungarian algorithm³², which has the algorithmic complexity of $O(m^3)$. If only the permutation matrix, \hat{f} , is known *a priori*, the parameters \hat{U} and $\hat{\mathbf{t}}$ can be computed using Horn’s algorithm³³ with complexity $O(m)$. Horn’s algorithm uses quaternions to provide a closed-form solution for aligning two point sets such that RMSD is minimized. If all of \hat{f} , \hat{U} , and $\hat{\mathbf{t}}$ are unknown, more sophisticated algorithms are required for minimizing RMSD between clusters of atoms. A good review of different techniques is provided in Ref. 27. For example, in Ref. 23, a two-stage method, which includes a Monte-Carlo perturbation, has been proposed for finding the global-minimum in RMSD. In Ref. 27, two efficient algorithms, GO-PERMDIST and FASTOVERLAP, were introduced. However, these techniques currently are limited to equal number of atoms in the model and the target. And, more importantly, the optimal translation $\hat{\mathbf{t}}$ that produces the best match is assumed to be known *a priori*. While this is a reasonable

approximation when $n = m$, determining the translational component is non-trivial when the two structures to compared have different number of atoms.

Here we present a new PPM algorithm based on graph theory arguments developed by McAuley and Caetano³⁴. This technique is general enough to be applied for systems with different number of atoms. And, as we will introduce in the following paragraphs, the similarity metric is defined such that the permutation function is the only argument over which the minimization has to be performed. Once the optimal permutation function \hat{f} is determined, Horn’s algorithm can be used to align efficiently the model to the target by finding \hat{U} and \hat{t} .

In Ref. 34, a graph representation of a point-set is used to identify the mapping f . The sets of points in the model \mathbf{M} and target \mathbf{T} can be expressed as graphs by using the information contained in the atom positions (nodes) and bonds (edges). Usually, a graph is defined by the set of nodes and edges (V, E) . We will, however, consider a graph \mathcal{G} to be a set of pairs of nodes, and say $(i, j) \in \mathcal{G}$ if an edge connecting nodes i and j is present in graph \mathcal{G} (using the notation developed in Ref. 34). The complete graphs, which contain all the possible edges in the point-set, representing the model and the target will be denoted by \mathcal{M} and \mathcal{T} , respectively.

Instead of using RMSD defined in Eq. 1, McAuley and Caetano introduced a metric that depends only on edge lengths and hence is invariant to rotations and translations. This metric, for a given permutation function f , is defined on the graphs and is provided in Eq. 2. The objective of the PPM technique is to determine the function \hat{f} that minimizes the metric $\mathcal{D}(f)$ as defined in Eq. 3.

$$\mathcal{D}(f) = \sum_{(i,j) \in \mathcal{M}} \left| d(\mathbf{r}_i^M, \mathbf{r}_j^M) - d(\mathbf{r}_{f(i)}^T, \mathbf{r}_{f(j)}^T) \right| \quad (2) \quad \hat{f} = \arg \min_{f: \mathcal{M} \rightarrow \mathcal{T}} \mathcal{D}(f) \quad (3)$$

The mapping \hat{f} produces a matching between the points in the model and the target, such that the sum of the differences in all the edge lengths is minimized. This definition allows for computing optimal mappings even in the presence of noise. The algorithms to determine \hat{f} fall under the class of quadratic assignment problems, which are in general NP-hard³⁵. In Ref 36, McAuley *et al.* introduced the concept of a rigid-graph to solve the matching problem in an efficient manner. A rigid-graph is a subset of the original graph such that the only transformations that can be applied to the node coordinates while preserving the distances in the rigid-graph are isometries (rigid-body translations and rotations). If the rigid-graph of the model \mathcal{M} is denoted by \mathcal{R} , then the new objective function can be written as:

$$\hat{f} = \arg \min_{f: \mathcal{R} \rightarrow \mathcal{T}} \mathcal{D}(f) \quad \text{where} \quad \mathcal{D}(f) = \sum_{(i,j) \in \mathcal{R}} \left| d(\mathbf{r}_i^M, \mathbf{r}_j^M) - d(\mathbf{r}_{f(i)}^T, \mathbf{r}_{f(j)}^T) \right| \quad (4)$$

where \mathcal{M} is replaced by the rigid-model-graph \mathcal{R} . The difference between \mathcal{M} and \mathcal{R} is the number of edges considered during the minimization. For example, a complete graph, where all the possible edges in the model point-set are considered to be a part of the graph, is shown in Figure 1 (a). In this complete graph, there are $m(m-1)/2 = O(m^2)$ edges. As defined in Ref. 34, the rigid graph for a two-dimensional (2D) point-set is constructed by first choosing two nodes that are connected by an edge. These two points are usually referred to as the *root nodes*. All the other points in the model are then connected to the two root nodes as shown in Figure 1 (b). Therefore, the rigid graph of the model contains the edges between the root nodes and, instead of all the edges in the model point-set, only those edges that connect the rest of the points to the root nodes. The total number of edges in this rigid graph is $2m-3 = O(m)$. The global rigidity theorem³⁷ implies that preserving the lengths of the edges in \mathcal{R} preserves the lengths in the complete graph of the model point-set. The required number of root nodes depends on the dimensionality of the point-set. In 2D, two root nodes are required and, in 3D, we need three root nodes to construct the rigid graph.

Ref. 34 contains complete details of the rigid-graph PPM algorithm. Here, we present figures that illustrate the steps in the algorithm in two dimensions. Figure 2(a, b) show the model and the target, respectively. The objective is to identify the set of points in the target that best match the model point-set.

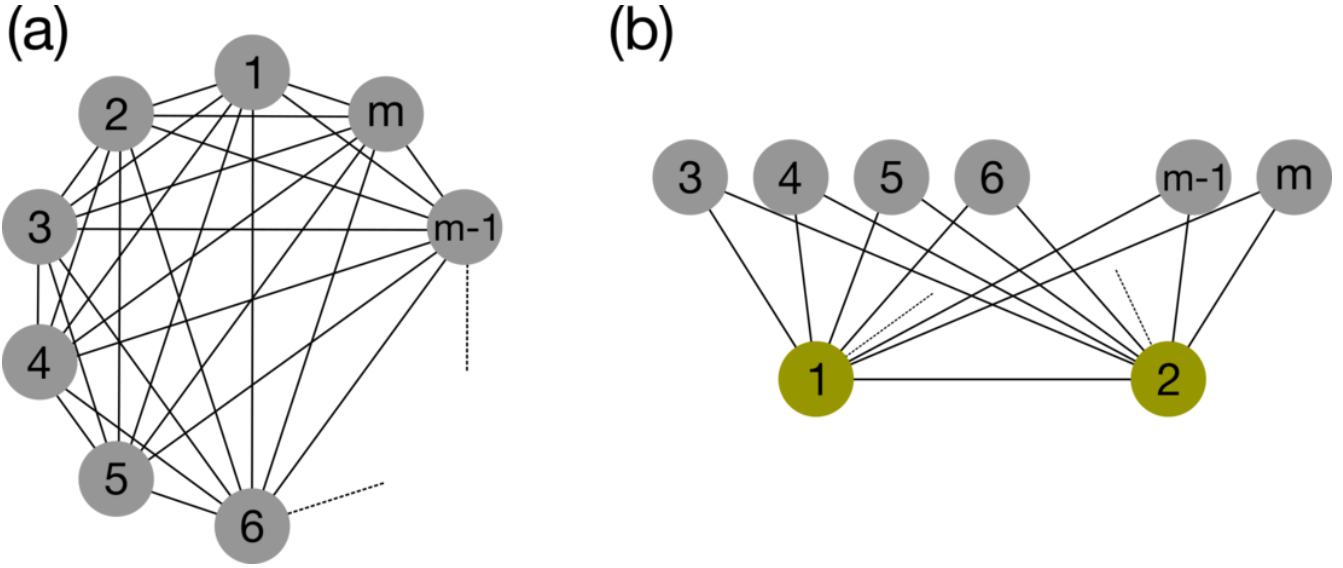


Figure 1. (a) A complete graph with all possible edges connecting the m points in the model is shown. In (b), the rigid-graph of the model is shown. The rigid graph in two dimensions consists of the edge between the two root nodes (highlighted) and all the edges between the rest of points and the root nodes.

1. The input for the PPM algorithm contains the two point-sets and the root nodes in the model. The choice of the root nodes does not influence the accuracy of the algorithm but if the root nodes are chosen judiciously, the run-time for obtaining the solution can be reduced. We are interested in minimizing the sum of differences in the edge lengths in the rigid graph of the model and the mapped point-set in the target (Eq. 4). We assume that these differences scale as the actual edge length. Therefore, picking the nodes that contain the largest edge as the root nodes can improve the efficiency of the algorithm. With this assumption, we choose the two nodes that are farthest apart as root nodes in 2D. The root nodes for the model are shown in Figure 2(c). In 3D, we choose three nodes where the sum of the edge lengths of the triangle is maximized.
2. Once the root nodes are fixed, we find all possible matches in the target for the root nodes. In 2D, the computational cost is $O(n^2)$. This is equivalent to enumerating all possible pairs of points in the target. In 3D the cost is $O(n^3)$ as three root nodes are required. Some of the matches for the root nodes in the target are shown in Figure 2(d). Consider the best match for the root nodes, as shown in Figure 3(a, b). A local coordinate system is defined with the root nodes in the model (Figure 3(a)) and the matched-root-nodes in the target (Figure 3(b)).
3. For each remaining point in the model, the vector in the local coordinate system is computed (as shown for two points in the model in Figure 3(c)). An equivalent vector in the target is then defined using the local coordinate system in the target (Figure 3(d)). A nearest-neighbor algorithm is then used to determine the point n_p that is closest to the equivalent vector in the target. For the two vectors in the model, equivalent vectors and the nearest points are shown in the target in Figure 3(d). The algorithmic complexity to determine the nearest point is $O(\log n)$ (using a KD-tree data-structure).

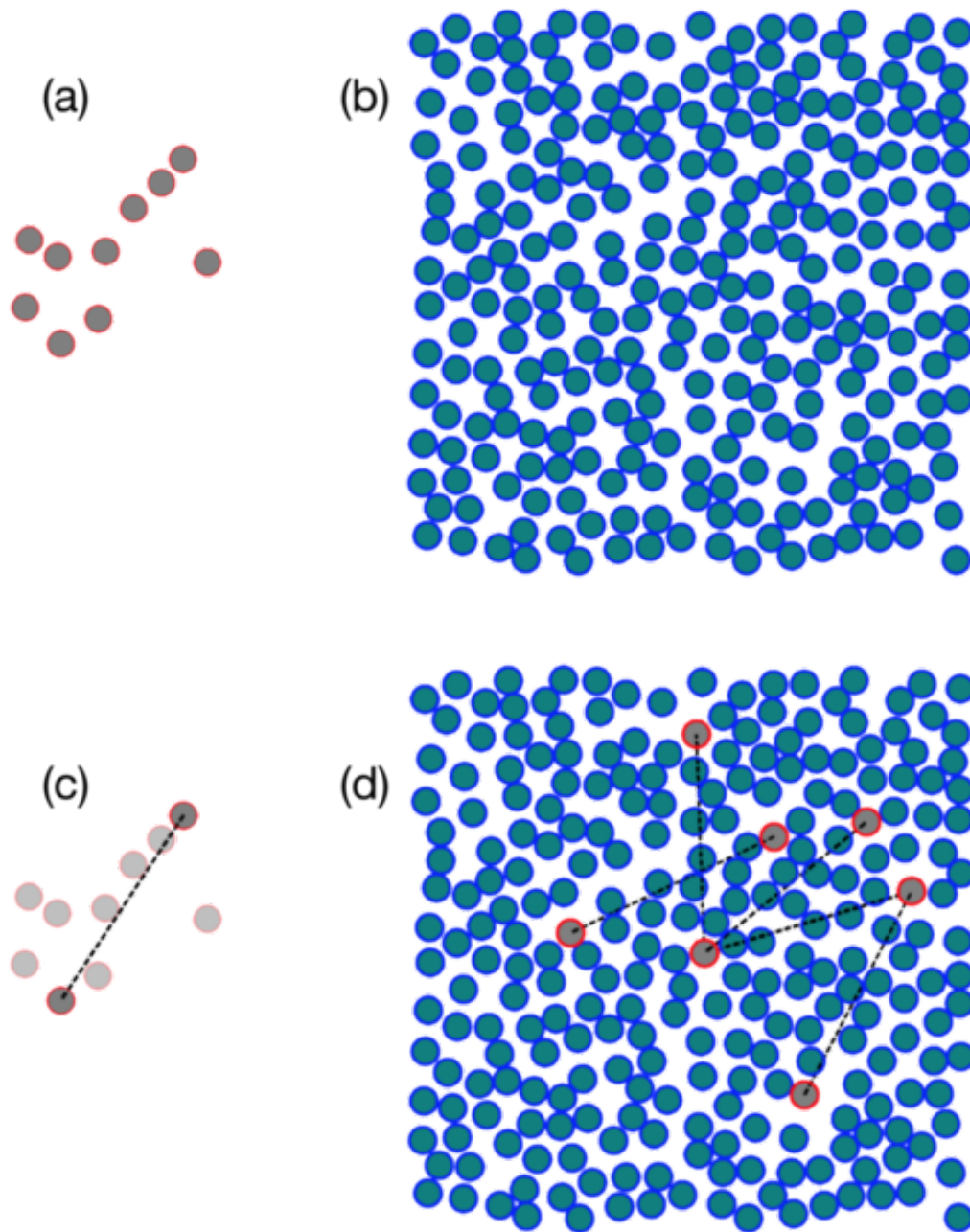


Figure 2. The model and target point-sets are shown in (a) and (b), respectively. The points are represented using discs to illustrate atoms in this example. In (c), the two root nodes in the model are highlighted. In (d), a few example pairs of points in the target that match the root nodes are illustrated.

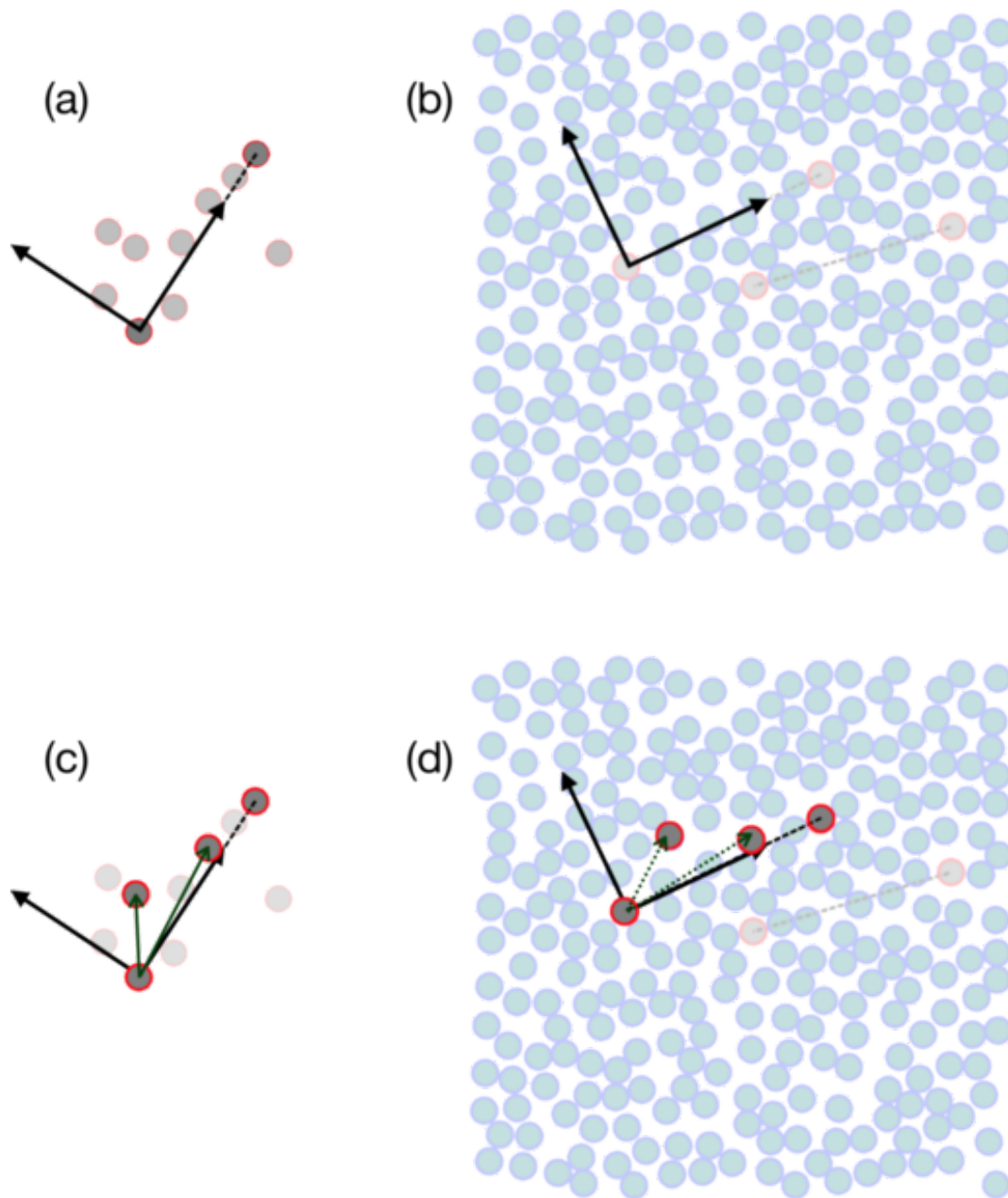


Figure 3. The local coordinate systems, defined by the root nodes, are illustrated in the model and the target in (a) and (b), respectively. In (c) the vectors of two points (other than the root nodes) in the model are shown and in (d) the equivalent vectors are shown using dotted lines. The highlighted points in (d) are the nearest-points to the equivalent vectors in the target.

4. Finally, the steps described above are repeated for all the remaining points in the model (Figure 4(a)). The points in the target that best match the model are shown in Figure 4(b).
5. In Figure 4(c), the alignment between the model and the mapped points are shown by overlapping points. To align the two point patterns, the rotation U and rigid body translation \mathbf{t} that minimizes the RMSD metric defined in Eq. 1 is computed using Horn's algorithm³³, which has a complexity of $O(m)$.

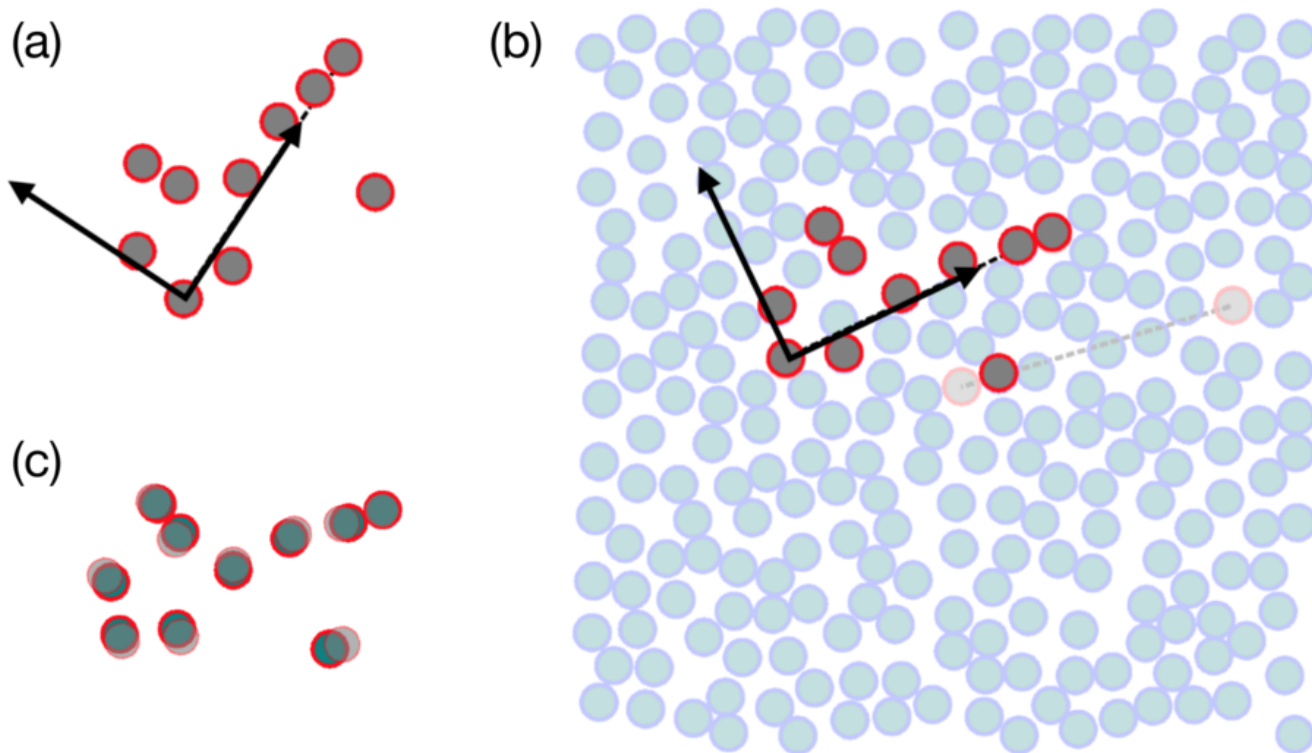


Figure 4. The model point-set with the local coordinate system is shown in (a). The best match found in the target point-set is shown in (b). In (c), the registration between the model and the mapped-points in the target, which is obtained using Horn's algorithm, is shown.

The complexity of the point pattern matching algorithm to compute \hat{f} is determined by combining the complexities in steps 1-3 and is given by $O(mn^d \log n)$, where $d = 2, 3, \dots$ is the dimensionality of the point-set. The Horn's algorithm in the last step adds an additional computational cost of $O(m)$ but the dominant terms come from the PPM algorithm. In Figure 5, we illustrate the complexity of the algorithm by comparing clusters of equal and unequal number of atoms, respectively. For the red curve, there are equal number of points in the model and target (i.e. $n = m$), and for the blue curve the number points in the model is fixed ($m = 10$) and the number of points in the target are varied. The target point-sets are created by picking random points in three-dimensions with the x , y and z coordinates in the interval $[-1, 1]$. The model set is created by picking a random subset of the target, adding a Gaussian random noise (with $\sigma = 0.1$) to the points, and randomizing the indices. The alignments are performed on a standard desktop computer (Intel Xeon quad-core processor, 1.80 GHz, 4 GB RAM) and the asymptotic scaling of $O(mn^3 \log n)$ for three-dimensional point-sets is shown in Figure 5. The PPM algorithm is coded in C++, with a Python wrapper to promote ease of use, and is shared online at <https://github.com/adehgha/ppm3d>. The python wrapper has been implemented with capabilities for parallelization on a distributed computing platform, such as HTCondor³⁸, for applications where millions of alignments have to be performed.

In summary, the PPM algorithm presented here can be used to obtain the permutation function between sets of atoms that minimizes the RMSD between the model and the target point-sets. The technique is particularly

useful when there are dissimilar number of atoms in the clusters being compared and the translation vector, $\hat{\mathbf{t}}$, that minimizes the RMSD parameter is unknown. The PPM algorithm can also be utilized when the extent of overlap between the model and the target point-sets is incomplete. That is, when there are outliers in the model point-set that do not match with points in the target. Such outliers are referred to as *occlusions*³⁹ in the image-processing literature. When occlusions are allowed, the PPM algorithm finds the largest subset of the model and the target that results in the best possible matching. This capability is particularly useful when there is limited overlap between the clusters being compared, e.g. when identifying binding regions between proteins^{40,41}.

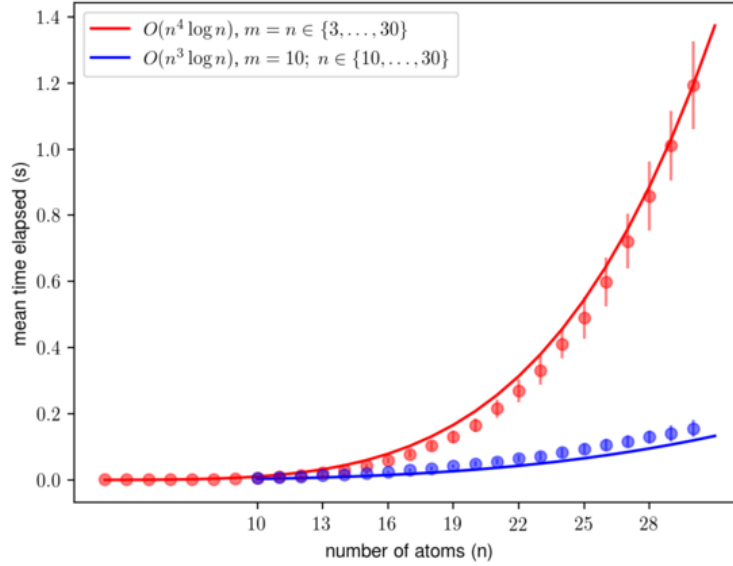


Figure 5. Performance scaling for the PPM algorithm as a function of the number of points in the model and target sets are shown. The tests are performed for equal number of points in both the model and target, i.e. $n = m$ and are shown in the red curve. The scaling with a fixed number of points in the model set ($m = 10$) and increasing number of points in the target is shown in the blue curve. The point sets are three-dimensional and the scaling is $O(mn^3 \log(n))$.

2 Results and Discussion

2.1 Local Atomic Motifs in Grain Boundaries - A Three-Dimensional Polyhedral Unit Model

Grain boundaries (GBs) are planar defects in polycrystalline materials and influence a wide array of structural and functional properties⁴². Unfortunately, GBs are also one of the least understood defect types in materials science. This is due to the vast and topologically complex, five-dimensional crystallographic degrees-of-freedom (DOF) of a GB^{43–45}. The five dimensions correspond to the so-called macroscopic degrees of freedom - three parameters define the misorientation between individual grains and the other two fix the boundary-plane orientation. These parameters constitute the bicrystallographic aspects of interfaces. Since the structure and properties of the GBs vary with the underlying bicrystallography, one of the primary objectives of grain boundary engineering has been to predict structure and properties from the five crystallographic parameters.

From a geometrical perspective, the structure of certain GBs (those with low-index planes at the interface) has been understood as clusters of atoms that form quasi-two-dimensional geometrical motifs. This model, referred to as the structural unit model (SUM), was first proposed by Bishop and Chalmers⁴⁶ and has been extended to a variety of tilt GBs by Sutton and Vitek^{47,48}. More recently, Han et al. developed a framework utilizing the metastable-SUM to predict GB structures and energies for [100] and [111] symmetric-tilt GBs⁴⁹. They emphasized that the metastable-

SUM framework can be used to describe structural variations in the complete five-dimensional crystallographic phase-space of GBs. One of the key steps in this framework relies on identifying pre-determined geometrical motifs in a variety of minimum-energy and metastable GB structures. However, identifying three-dimensional geometrical motifs in complex, disordered GBs is difficult. The PPM algorithm is uniquely suited to address this issue.

In this article, rather than focusing on the physical aspects of GB properties, we show a simple example to illustrate how the PPM algorithm can be used to better understand GB structures. We will also use the recently developed technique, by Banadaki and Patala⁵, for identifying three-dimensional geometrical motifs (polyhedral-units), as it provides a more robust description of the building blocks of GBs. In Ref 5 we showed that 11-atom polyhedra, which can be viewed as distorted octadecahedra¹, are observed in two of the [100] symmetric-tilt GBs analyzed in aluminum. Specifically, these are the $\Sigma 5$ ($0\bar{2}1$) and $\Sigma 5$ ($0\bar{1}3$) GBs and their atomistic structures are shown in Figure 6. In 6(e), the 11-atom polyhedral units are compared with the perfect octadecahedra and the RMSD for the $\Sigma 5$ ($0\bar{2}1$) and $\Sigma 5$ ($0\bar{1}3$) units are found to be 0.5 and 0.4, respectively. Their mutual RMSD is 0.17, which is significantly lower.

In Figure 7, the energies of all the [100] symmetric tilt GBs in aluminum are shown as a function of tilt angle. The two $\Sigma 5$ GBs are highlighted and correspond to cusps in this set of symmetric tilts. We will use these two *delimiting* GBs⁴⁹ as references and compare them with the structure of the neighboring GBs as the tilt angle is varied between 36.87° and 53.13° . That is, we start with the octadecahedra observed in the two $\Sigma 5$ GBs and use the PPM algorithm to identify similar atomic motifs in the boundaries between the two cusps. We analyzed the structures of the four GBs highlighted in the inset of Figure 7. The GB structures of $\Sigma 29$ ($0\bar{2}5$) and $\Sigma 29$ ($0\bar{7}3$) are shown in Figure 8. The structures of $\Sigma 73$ ($0\bar{3}8$) and $\Sigma 73$ ($0\bar{1}15$) are shown in Figures S1 and S2, respectively, in the Supplementary Information (SI).

As can be observed from the structures in Figure 8, the variations in the tilt angles are accommodated by adding “gaps” between the octadecahedra units. These gaps correspond to the **D** structural unit (from the perspective of SUM) or the dual-tetrahedra (from the perspective of polyhedral unit model⁵). The SUM representations for all the GBs analyzed in this article are shown in Figure S3 of the SI as reference. We performed a similar structural analysis of the $\Sigma 73$ GBs in the SI. This simple example illustrates the capability of the PPM algorithm for comparing GB structures, as the crystallographic DOF are varied, in an automated manner.

In addition to identifying the relevant units, the similarity metric provides a way to compute the distortions in the geometrical motifs. In the SUM model, the structure of a GB that is located between two delimiting boundaries contains minority structural units that correspond to the (secondary) dislocations or *disconnections*⁵¹. For example, in the $\Sigma 29$ GBs, these minority units correspond to the **D** SU. The disconnection model provides a physical basis for the distortions of the 11-atom units – they are caused by the strain fields associated with the disconnection defects in the GB. To illustrate the distortions, we plotted the RMSD of the 11-atom units, with respect to the units observed in the delimiting $\Sigma 5$ GBs, as a function of the tilt angle in Figure 9.

To better appreciate the physical significance of comparing GB structures using methods like PPM, readers are referred to the recent article by Han et al.⁴⁹ and prior work by Sutton, Balluffi, Vitek, and co-authors^{47,48,52,53}. For example, in Ref 49, using the metastable-SUM model, Han et al. showed that interfacial energies can be predicted for the [100] and [111] symmetric tilt GBs in BCC tungsten, over the entire misorientation range, based on atomistic simulations of only four delimiting GBs. In Ref 52, Balluffi proposed a simple model for predicting GB properties, such as diffusivity, using the SUM and the properties of the delimiting interfaces. Therefore, the ability to express the structure of vicinal GBs as combinations of polyhedral units that are characteristic of certain low-energy, delimiting GBs can lead to quantitative crystallography-structure-property relationships for interfaces in the complete five-dimensional crystallographic phase-space. Traditionally, the SUM has only been applied for a few cases of symmetric tilt/twist GBs. We anticipate that a combination of the three-dimensional polyhedral unit model⁵ and the PPM algorithm described in this article will help advance this structural framework to more complex GBs with mixed crystallographic character.

¹This polyhedron is more precisely referred to as the Edge-Contracted-Icosahedron (ECI)⁵⁰. In chemistry, however, the ECI is most commonly called the octadecahedron, for 18 triangular faces.

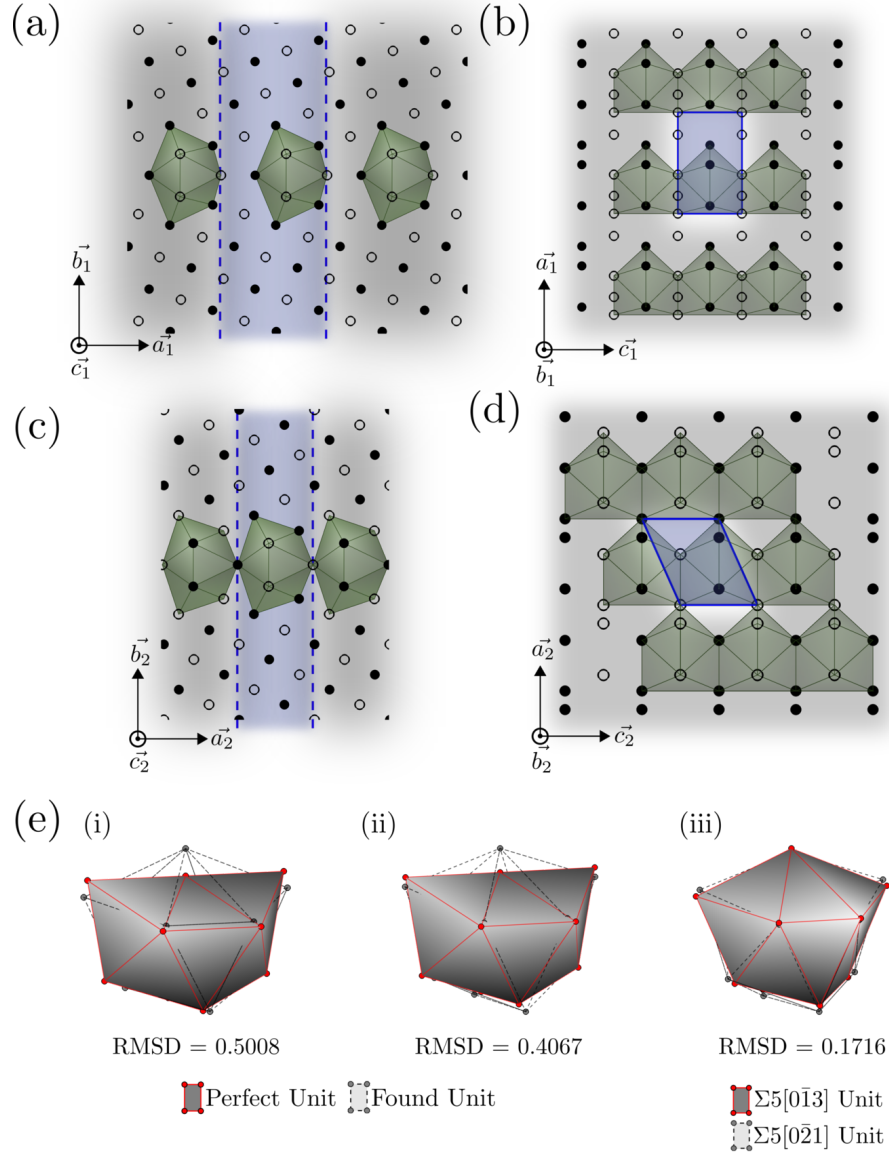


Figure 6. The atomistic structure of $\Sigma 5(0\bar{1}3)$ and $\Sigma 5(0\bar{2}1)$ with the 11-atom polyhedral units highlighted are shown. The views in (a, c) are along the tilt axis, $[100]$, and (b, d) are along the boundary-plane normal. In (e) the RMSD of the observed polyhedral units are shown when compared with the perfect octadecahedra and when compared with each other. The “Found Unit“ in the legend of (e, i) and (e, ii) refers to the unit observed in the $\Sigma 5(0\bar{2}1)$ and $\Sigma 5(0\bar{1}3)$ GBs, respectively. The axes in the (a, b) are such that, $\vec{a}_1 = [031]$, $\vec{b}_1 = [0\bar{1}3]$ and $\vec{c}_1 = [100]$. The axes in (c, d) are, $\vec{a}_2 = [012]$, $\vec{b}_2 = [0\bar{2}1]$ and $\vec{c}_2 = [100]$.

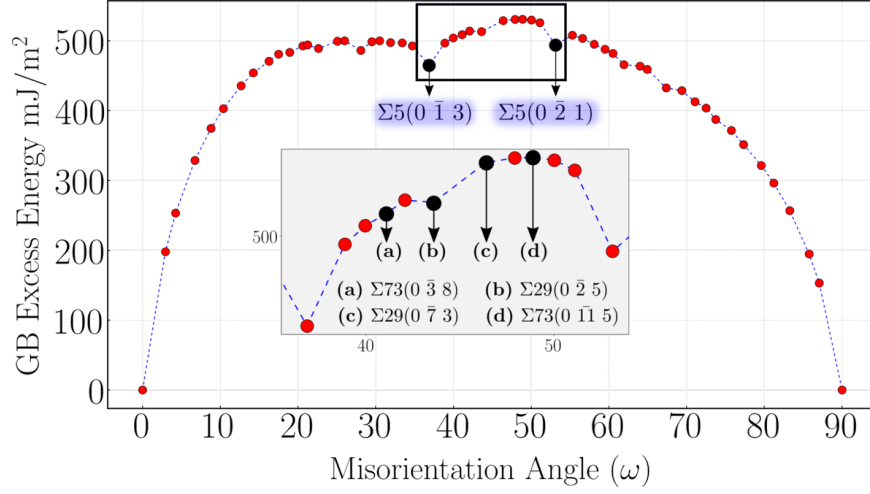


Figure 7. The energies of the $[100]$ symmetric tilt GBs of Aluminum are shown along with the GBs analyzed in this article. The $\Sigma 5$ GBs correspond to the delimiting interfaces used as reference to compare the structures of the GBs marked as (a), (b), (c), and (d).

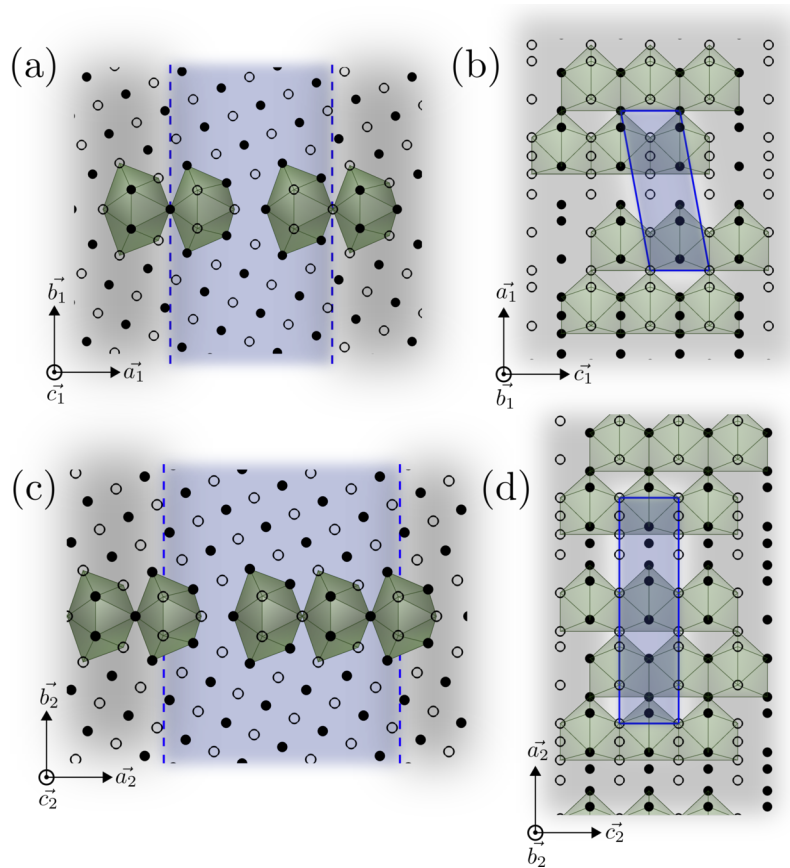


Figure 8. The atomistic structure of $\Sigma 29 (0\bar{2}5)$ and $\Sigma 29 (0\bar{7}3)$ are shown, with the 11-atom polyhedral units highlighted, in (a, b) and (c, d). The views in (a, c) are along the tilt axis and (b, d) are along the boundary-plane normal. The axes in the (a, b) are such that, $\vec{a}_1 = [052]$, $\vec{b}_1 = [0\bar{2}5]$ and $\vec{c}_1 = [100]$. The axes in (c, d) are, $\vec{a}_2 = [037]$, $\vec{b}_2 = [0\bar{7}3]$ and $\vec{c}_2 = [100]$.

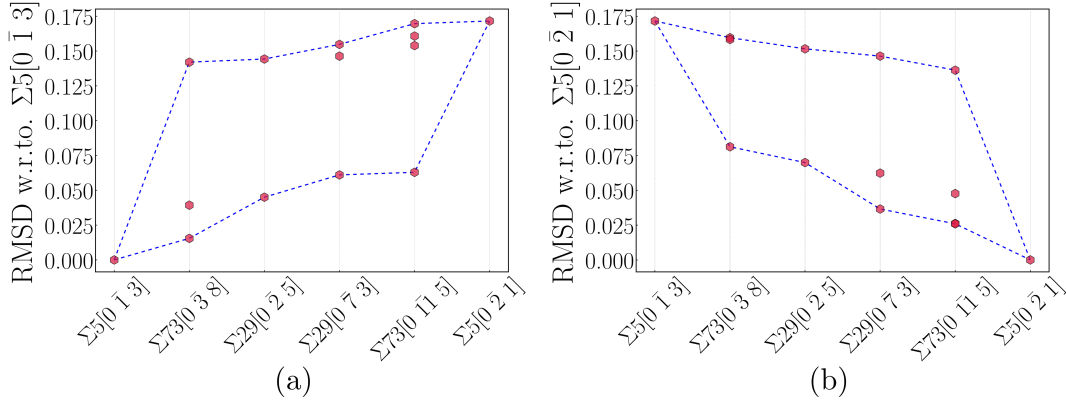


Figure 9. The RMSD values of the observed 11-atom units when compared to the units observed in the reference, delimiting, $\Sigma 5$ GBs are plotted. In (a) and (b), the units are compared to the corresponding unit in the $\Sigma 5 (0\bar{1}3)$ and the $\Sigma 5 (0\bar{2}1)$ GBs, respectively.

2.2 Local Structure in Metallic Glasses - The Quasi-Icosahedral Clusters

Metallic glasses (MGs) are disordered materials, and their lack of long-range translational symmetry necessitates a rigorous understanding of their short- and medium-range order (SRO and MRO) structure. SRO in MGs is comprised of an atom and its nearest neighbors, henceforth called a *cluster*. SRO balances efficient packing on one hand and chemical ordering on the other⁵⁴. Efficient packing of clusters without long-range translational symmetry requires the structure of the material to be disrupted, and therefore identifying the structural units that cause this disruption and lack of connectivity at the short-range length scale is of considerable interest. For example, in Zr-Cu based MGs icosahedra with 5-fold symmetry (which cannot tile 3D space) are the dominant SRO structural motifs^{55–58}. Additionally, recent studies have shown that the distribution of clusters such as icosahedra can have a profound influence on the mechanical properties of bulk metallic glasses¹. For further information, a review on MG structure can be found in Ref 57.

Characterization of clusters in MGs is done most often using Voronoi indices, the p-vector of the number of three-, four-, five-, and six-sided faces. For example, in Zr-Cu based glasses, the atoms with icosahedral SRO are identified as those with Voronoi indices $\langle 0\ 0\ 12\ 0 \rangle$. However, the clusters will not have a perfect icosahedral geometry due to the inherent disorder in the glass. In addition, previous studies classified some Voronoi indices with a high number of pentagonal faces and geometry intuitively related to an icosahedron as *quasi-icosahedral*⁵⁵. However, while the quasi-icosahedral Voronoi polyhedra resemble an icosahedron, a quantitative basis for this consideration is lacking due to the topological nature of the Voronoi method.

Here, we employ the PPM algorithm to analyze the atomic structure of a $\text{Zr}_{50}\text{Cu}_{45}\text{Al}_5$ model glass to address the questions:

1. How distorted are the clusters with Voronoi topology $\langle 0\ 0\ 12\ 0 \rangle$, when compared to a geometrically perfect icosahedron? and
2. How similar are the clusters whose Voronoi polyhedra have a high number of 5-sided faces (some of which are considered quasi-icosahedral) to a perfect icosahedron?

The $\text{Zr}_{50}\text{Cu}_{45}\text{Al}_5$ model used in this work was obtained by quenching a liquid with that composition with 9,826 atoms from 2000 K to 600 K at 5×10^{10} K/s using molecular dynamics in LAMMPS⁵⁹ using the Sheng embedded atom model potential⁵⁸, updated in 2012. After quenching, the glass was equilibrated for 500 ps and the inherent structure was calculated by performing a conjugate gradient minimization of the potential energy. We extracted every cluster from this model. The Voronoi index distribution of these clusters is identical to those of other models produced by the same potential⁵⁸. The coordination number distribution of the clusters is shown in Figure 10(a).

Coordination number twelve is the most common, consistent with icosahedral SRO. For each cluster, the bond lengths from the center atom to its nearest neighbors were normalized so their average value was 1.0, then each cluster was compared to a perfect icosahedron using PPM.

After alignment, three metrics in addition to the objective function, RMSD, were calculated for each cluster comparing it to the perfect icosahedron: L^1 , L^{inf} , and a measure of angular variance, V_A . In this section we refer to RMSD as L^2 to highlight the connection between RMSD, L^1 , and L^{inf} . These metrics are defined by:

$$\begin{aligned} L^1(\mathbf{M}, \mathbf{T}) &= \frac{1}{m} \sum_{i=1}^m |\hat{\mathbf{r}}_i^M - \mathbf{r}_{f(i)}^T| \\ L^{inf}(\mathbf{M}, \mathbf{T}) &= \max(\hat{\mathbf{r}}_i^M - \mathbf{r}_{f(i)}^T) \\ V_A(\mathbf{M}, \mathbf{T}, c) &= \frac{1}{N} \sum_{n=i,j}^N |\angle(\hat{\mathbf{r}}_i^M, \mathbf{0}, \hat{\mathbf{r}}_j^M) - \angle(\mathbf{r}_{f(i)}^T, \mathbf{0}, \mathbf{r}_{f(j)}^T)| \end{aligned} \quad (5)$$

where m is the number of points in the model and target, $\hat{\mathbf{r}}_i^M = U\mathbf{r}_i^M + \mathbf{t}$ is the position of point i in the model point-set after rotation and translation, and the \max in L^{inf} runs over the indices $i \in [1, m]$. N is the number of neighbors (bonds) in the model where two points are neighbors if they are within a distance c of one another, $\angle(\cdot, \mathbf{0}, \cdot)$ is the angle between a pair of points going through the center of the point-set, and the summation over $n = i, j$ in V_A includes all pairs of neighbors in the point-set. In this work we define neighbors using the cutoff $c = 3.6 \text{ \AA}$, which is the first minimum in the total radial distribution function.

These four metrics were chosen to quantify various aspects of the differences in atomic structure as well as to illustrate the ability to calculate various structural similarity metrics after alignment by PPM. L^1 puts less emphasis on outliers (poorly matching atoms in the model and the target) than L^2 , while L^{inf} only considers the worst outlier. V_A provides a measure of angular variation to complement the bond length measures of the L^p metrics. The geometric mean of these four metrics, $\sqrt[4]{L^2 \cdot L^1 \cdot L^{inf} \cdot V_A}$, was used as the final metric of comparison to the perfect icosahedron and is henceforth called the geometric mean error (GME). GME has more discriminating power than RMSD (L^2) alone. The geometric mean is appropriate for calculating averages of numbers with different numerical ranges and retains information about the relative change of those numbers when comparing different values.

We first consider all 2,285 clusters with coordination number 12 after alignment to a target of a perfect icosahedron. Figure 10(b) (blue) shows the distribution of the GMEs calculated after these alignments. The distribution is bimodal, and the low-GME peak is composed of geometrically icosahedral clusters. GME histograms for clusters with Voronoi indices $\langle 0 0 12 0 \rangle$, $\langle 0 2 8 2 \rangle$, or $\langle 0 3 6 3 \rangle$ (orange, green, and red, respectively) illustrate the range of GME values associated with clusters with these different topologies.

Figure 11 shows the mean and standard deviations of the GME for clusters with the most common topologies, categorized by their Voronoi indices. Not all of these clusters have coordination number 12, but all the clusters were aligned to a perfect icosahedron, regardless. The clusters with Voronoi indices $\langle 0 0 12 0 \rangle$ are most geometrically similar to the perfect icosahedron, consistent with the MG literature, as shown by their notably low mean GME. The Voronoi indices that are most often considered quasi-icosahedral include $\langle 0 2 8 2 \rangle$, $\langle 0 2 8 1 \rangle$, and $\langle 0 1 10 2 \rangle$ ^{57,60–63}, and while many of the clusters with these topologies exhibit a low GME, they display a wide range of distortions. In addition, the mean GME of clusters with Voronoi index $\langle 0 3 6 3 \rangle$ is 0.57. This value is significantly larger than the dip between the two peaks in the total histogram in Figure 10(b) at 0.42, so these clusters should not be classified as quasi-icosahedral based on their geometry. Clusters with VI $\langle 0 0 12 0 \rangle$ or $\langle 0 2 8 2 \rangle$ and GME greater than 0.42 tend to be Zr-centered (83% and 62%, respectively). This indicates that Zr-centered clusters with icosahedral topology tend to be more distorted than Cu- or Al- centered clusters with icosahedral topology, consistent with previous findings⁵⁸. The average composition of the nearest-neighbor shells of these same clusters is similar to the overall composition of the model, so there are no compositional abnormalities in the shells of these clusters.

The distribution of GME for $\langle 0 2 8 2 \rangle$ topology clusters (green in Figure 10(b)) straddles this 0.42 dividing line between icosahedral and non-icosahedral geometries, despite being widely considered quasi-icosahedral in the MG literature^{57,60–63}. Figure 12 illustrates the geometrical disparity between two $\langle 0 2 8 2 \rangle$ clusters. The $\langle 0 2 8 2 \rangle$ cluster

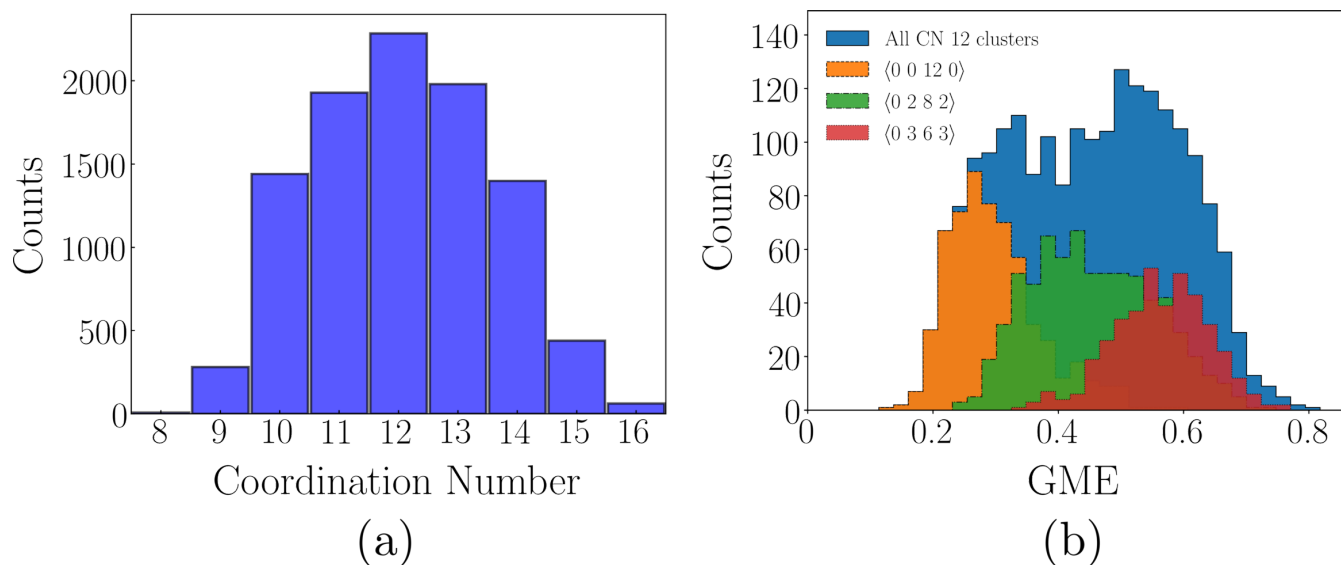


Figure 10. (a) The coordination number distribution for the $\text{Zr}_{50}\text{Cu}_{45}\text{Al}_5$ metallic glass model studied in this section. (b) The bimodal distribution (blue) of GMEs for all 2,285 clusters with coordination number 12 in the MG model. The colors show analogous histograms for the sets of clusters with three different Voronoi indices, all of which have coordination number 12.

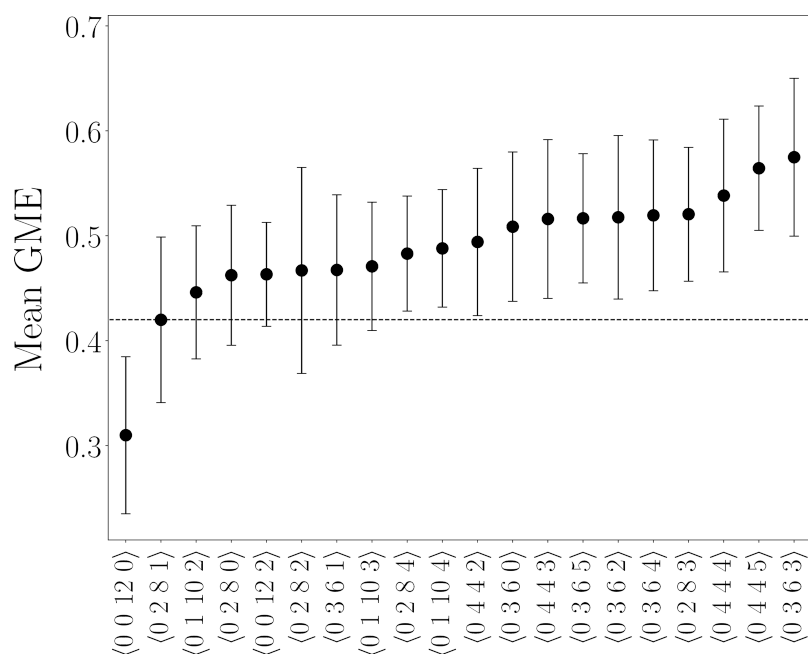


Figure 11. The mean of the GME for clusters with specific Voronoi indices with a high number of pentagonal faces. The clusters with Voronoi index $\langle 0 0 12 0 \rangle$ are well below the cutoff of 0.42, while clusters with Voronoi index $\langle 0 3 6 3 \rangle$ are well above the cutoff and are therefore do not have icosahedral geometry despite their high number of pentagonal faces and coordination number of 12. The error bars show one standard deviation of the GME values. The horizontal dotted line designates the GME cutoff of 0.42.

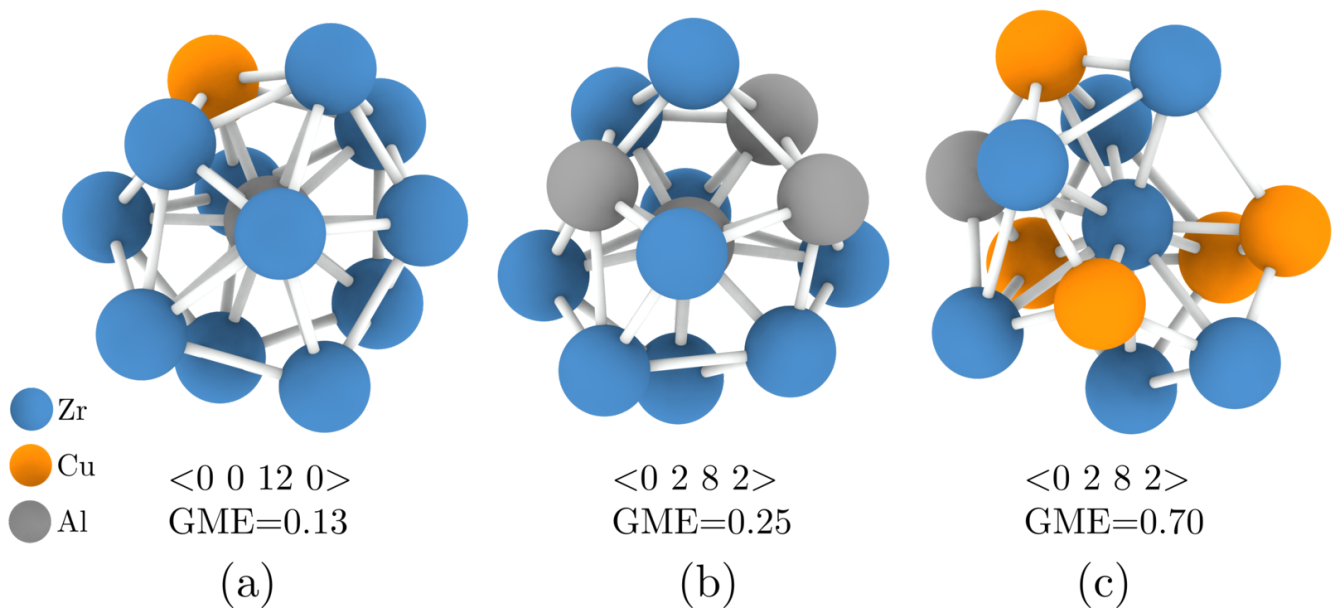


Figure 12. Three clusters illustrate the topological insufficiency of Voronoi indices to differentiate the geometry of the structures, while the GME provides sufficient descriptive power. A $\langle 0\ 0\ 12\ 0 \rangle$ cluster (a) with low GME has similar structure to a $\langle 0\ 2\ 8\ 2 \rangle$ cluster (b) with low GME, but different structure than another $\langle 0\ 2\ 8\ 2 \rangle$ cluster (c) with high GME.

in Figure 12(b) has a low GME of 0.25 and has similar structure to both the perfect icosahedron and the Figure 12(a) cluster with $\langle 0\ 0\ 12\ 0 \rangle$ topology and GME 0.13 (Figure 12(a)). However, the $\langle 0\ 2\ 8\ 2 \rangle$ cluster in Figure 12(c) has a large GME of 0.70 and is dissimilar in structure to both previous clusters.

These results answer the two questions above. $\langle 0\ 0\ 12\ 0 \rangle$ topology is strongly associated with icosahedral geometry, as shown by the histogram in orange in Figure 10(b), almost all of which falls in the low-GME peak of the total distribution below the 0.42 cutoff. As illustrated in Figure 11, many of the $\langle 0\ 2\ 8\ 1 \rangle$ topology clusters are geometrically similar to a perfect icosahedron, as are many clusters with $\langle 0\ 1\ 10\ 2 \rangle$ and $\langle 0\ 2\ 8\ 2 \rangle$ topologies. However, some clusters with the latter Voronoi indices have a GME that falls above the geometrically-icosahedral cutoff of 0.42 and should not be classified as having icosahedral geometry; Figure 12(c) shows a specific example. $\langle 0\ 3\ 6\ 3 \rangle$ topologies, despite having a fairly large fraction of 5-sided faces and being sometimes considered quasi-icosahedral in the literature^{61,63} do not have icosahedral geometry based on their GME histogram. In general, PPM alignment and the GME score provides a quantitative measure of how icosahedral a cluster is in a way that Voronoi indices as a measure of topology do not. PPM and GME is a particularly useful discriminator for topologies reported to correspond to distorted, quasi-icosahedral structures.

The question of whether geometry or topology is more important for determining the influence of structure on the properties and processes of metallic glasses remains to be answered. Icosahedral topology is considered important because plastic deformation tends to avoid regions in the structure with a high concentration of icosahedral topology⁶⁴; icosahedral topology regions in the supercooled liquid have slower local dynamics than other topologies^{65,66}; and the concentration of icosahedral topology increases significantly as the liquid cools through the glass transition^{57,65,66}. However, the energy of clusters depends more on their geometry (bond lengths, bond angles, coordination numbers) than on their topology, so we speculate that the explanatory power of topology arises because it is a proxy for geometry that is robust against disorder and easy to compute. PPM provides a robust, computable method of assessing geometry; future work will test its explanatory power for properties and processes in metallic glass systems.

3 Conclusions

We have presented a point-pattern matching algorithm for local structural analysis in atomistic simulations. The PPM algorithm relies on matching the edges in the model point-set with those in the target. The algorithm is made reasonably efficient by reducing the number of edge-lengths to be matched, represented by a rigid-graph, and by using the k -nearest neighbor algorithm for identifying similar points in the model and the target. The complexity of the algorithm for matching point sets in three-dimensions is $O(mn^3 \log n)$, where m and n are the number of points in the model and the target, respectively.

While there exist efficient algorithms for matching sets of atoms²⁷, these techniques generally assume that the optimal translation required to minimize RMSD is known *a priori*. However, when $\hat{\mathbf{t}}$ is unknown, the PPM algorithm is necessary to determine the optimal matching between the model and target point sets. Examples of such analyses are provided in section 2.1, where we had identified pre-defined geometrical motifs (the model) in GB structures (the target) between the two delimiting $\Sigma 5$ grain boundaries and in section 2.2, where we investigated the quasi-icosahedral topologies in the atomistic structure of metallic glasses.

PPM should find applications in the study of a variety of materials-science/chemistry phenomena. For example, in grain boundary science and engineering, the concept of coincidence site lattices (CSLs)⁶⁷ and their corresponding Σ -misorientations play a fundamental role in the analysis of interfaces both in experiments and simulations. The PPM algorithm can be utilized to systematically identify coincidence (match) between sub-lattices that generate the CSLs. Additionally, the PPM algorithm can help identify geometric relationships that lead to *near*-coincidence between lattices. The near-CSLs are particularly useful for identifying preferred orientation relationships between dissimilar materials⁶⁸. In metallic glasses, PPM could be used to test the hypotheses that other, non-icosahedral structures with non-crystallographic symmetry like tri-capped trigonal prisms are present in glass-forming alloys that do not exhibit icosahedra⁶⁹, and more generally to investigate the role of geometry as opposed to topology on processes like the glass transition and plastic deformation and properties like the glass transition and ductility.

Beyond the systems studied here, the determination of the structure of nano-clusters and the reaction pathways as these clusters change shape, grow or dissolve is of great interest in nano- and biological-sciences. The PPM algorithm can be used to systematically identify the changes in atomistic structures when modeling the growth of clusters or mutations in polymeric/protein molecules^{70–73}. As mentioned in section 1.1, another unique capability of the PPM algorithm is that one can allow for outliers (or occlusions) in the model point-set. This capability will be particularly useful when one is not aware of the appropriate model unit. When occlusions are allowed, the PPM algorithm finds the largest subset of the model and the target that gives the best possible matching. When combined with an unsupervised learning algorithm, this capability can help identify atomic motifs¹⁸ that are common across large clusters of atoms.

Finally, it is of interest to improve the computational efficiency of the algorithm while being able to find the global-minima in the pattern matching. For example, a recently proposed technique, termed Go-ICP⁷⁴ might provide similar results with better scaling with the size of the target. There is, however, a computational overhead as the optimization is performed in the space of rotations and translations (denoted by the group $SE(3)$). Therefore, we anticipate that for smaller cluster sizes, the PPM algorithm will more appropriate. An open-source implementation of PPM suitable for atomistic materials simulations and parallelized computation is hosted on GitHub at <https://github.com/spatala/ppm3d>.

Acknowledgements

Development of the PPM approach and application to grain boundaries by AB and SP was supported by the Air Force Office of Scientific Research Young Investigator Program funded through the Aerospace Materials for Extreme Environments (Contract # FA9550-17-1-0145). Computing resources for generating grain boundary structures was provided by the High Performance Computing Center at North Carolina State University. Implementation of the python wrapper and parallelization and application to metallic glasses by JJM and PMV was supported by NSF DMR-1332851, then by NSF DMR-1728933. The computing for parts of this research was performed using the compute resources and assistance of the UW-Madison Center for High Throughput Computing (CHTC)

in the Department of Computer Sciences. The CHTC is supported by UW-Madison, the Advanced Computing Initiative, the Wisconsin Alumni Research Foundation, the Wisconsin Institutes for Discovery, and the National Science Foundation, and is an active member of the Open Science Grid, which is supported by the National Science Foundation and the U.S. Department of Energy's Office of Science.

References

1. Ding, J., Patinet, S., Falk, M. L., Cheng, Y. & Ma, E. Soft spots and their structural signature in a metallic glass. *Proceedings of the National Academy of Sciences* **111**, 14052–14056 (2014).
2. Lazar, E. A., Han, J. & Srolovitz, D. J. Topological framework for local structure analysis in condensed matter. *Proceedings of the National Academy of Sciences* **112**, E5769–E5776 (2015).
3. Barnette, D. On p-vectors of 3-polytopes. *Journal of Combinatorial Theory* **7**, 99–103 (1969).
4. Lazar, E. A., Mason, J. K., MacPherson, R. D. & Srolovitz, D. J. Complete topology of cells, grains, and bubbles in three-dimensional microstructures. *Physical review letters* **109**, 095505 (2012).
5. Banadaki, A. D. & Patala, S. A three-dimensional polyhedral unit model for grain boundary structure in fcc metals. *npj Computational Materials* **3**, 13 (2017).
6. Chang, S.-H., Cheng, F.-H., Hsu, W.-H. & Wu, G.-Z. Fast algorithm for point pattern matching: invariant to translations, rotations and scale changes. *Pattern recognition* **30**, 311–320 (1997).
7. Myers, R., Wison, R. & Hancock, E. R. Bayesian graph edit distance. *IEEE Transactions on Pattern Analysis and Machine Intelligence* **22**, 628–635 (2000).
8. Carcassoni, M. & Hancock, E. R. Spectral correspondence for point pattern matching. *Pattern Recognition* **36**, 193–204 (2003).
9. Wang, H. & Hancock, E. R. A kernel view of spectral point pattern matching. In *Joint IAPR International Workshops on Statistical Techniques in Pattern Recognition (SPR) and Structural and Syntactic Pattern Recognition (SSPR)*, 361–369 (Springer, 2004).
10. Goodrich, M. T., Mitchell, J. S. & Orletsky, M. W. Approximate geometric pattern matching under rigid motions. *IEEE Transactions on Pattern Analysis and Machine Intelligence* **21**, 371–379 (1999).
11. Caetano, T. S., McAuley, J. J., Cheng, L., Le, Q. V. & Smola, A. J. Learning graph matching. *IEEE transactions on pattern analysis and machine intelligence* **31**, 1048–1058 (2009).
12. Martin, Y. C. *et al.* A fast new approach to pharmacophore mapping and its application to dopaminergic and benzodiazepine agonists. *Journal of computer-aided molecular design* **7**, 83–102 (1993).
13. Finn, P. W. *et al.* Rapid: Randomized pharmacophore identification for drug design. In *Proceedings of the thirteenth annual symposium on Computational geometry*, 324–333 (ACM, 1997).
14. Murtagh, F. A new approach to point pattern matching. *Publications of the Astronomical Society of the Pacific* **104**, 301 (1992).
15. Weber, G., Knipping, L. & Alt, H. An application of point pattern matching in astronautics. *Journal of Symbolic Computation* **17**, 321–340 (1994).
16. Akutsu, T., Kanaya, K., Ohyama, A. & Fujiyama, A. Point matching under non-uniform distortions. *Discrete Applied Mathematics* **127**, 5–21 (2003).
17. Nussinov, R. & Wolfson, H. J. Efficient detection of three-dimensional structural motifs in biological macromolecules by computer vision techniques. *Proceedings of the National Academy of Sciences* **88**, 10495–10499 (1991).
18. Maldonis, J. J., Banadaki, A., Patala, S. & Voyles, P. M. Short-range order structure motifs learned from an atomistic model of a zr50cu45al5 metallic glass. *In Preparation*.
19. Salvi, J., Matabosch, C., Fofi, D. & Forest, J. A review of recent range image registration methods with accuracy evaluation. *Image and Vision computing* **25**, 578–596 (2007).
20. Goshtasby, A. A. *Image registration: Principles, tools and methods* (Springer Science & Business Media, 2012).

21. Coutsias, E. A., Seok, C. & Dill, K. A. Using quaternions to calculate rmsd. *Journal of computational chemistry* **25**, 1849–1857 (2004).
22. Bartók, A. P., Payne, M. C., Kondor, R. & Csányi, G. Gaussian approximation potentials: The accuracy of quantum mechanics, without the electrons. *Physical review letters* **104**, 136403 (2010).
23. Sadeghi, A. *et al.* Metrics for measuring distances in configuration spaces. *The Journal of chemical physics* **139**, 184118 (2013).
24. Ferré, G., Maillet, J.-B. & Stoltz, G. Permutation-invariant distance between atomic configurations. *The Journal of chemical physics* **143**, 104114 (2015).
25. Behler, J. Perspective: Machine learning potentials for atomistic simulations. *The Journal of chemical physics* **145**, 170901 (2016).
26. De, S., Bartók, A. P., Csányi, G. & Ceriotti, M. Comparing molecules and solids across structural and alchemical space. *Physical Chemistry Chemical Physics* **18**, 13754–13769 (2016).
27. Griffiths, M., Niblett, S. P. & Wales, D. J. Optimal alignment of structures for finite and periodic systems. *Journal of chemical theory and computation* **13**, 4914–4931 (2017).
28. Temelso, B., Mabey, J. M., Kubota, T., Appiah-Padi, N. & Shields, G. C. Arbalign: A tool for optimal alignment of arbitrarily ordered isomers using the kuhn–munkres algorithm. *Journal of chemical information and modeling* **57**, 1045–1054 (2017).
29. Imbalzano, G. *et al.* Automatic selection of atomic fingerprints and reference configurations for machine-learning potentials. *The Journal of Chemical Physics* **148**, 241730 (2018).
30. Musil, F. *et al.* Machine learning for the structure–energy–property landscapes of molecular crystals. *Chemical Science* (2018).
31. Rudin, W. Principles of mathematical analysis. chap. 2, 30–36 (1976).
32. Kuhn, H. W. The hungarian method for the assignment problem. *Naval Research Logistics (NRL)* **2**, 83–97 (1955).
33. Horn, B. K. Closed-form solution of absolute orientation using unit quaternions. *JOSA A* **4**, 629–642 (1987).
34. McAuley, J. J. & Caetano, T. S. Fast matching of large point sets under occlusions. *Pattern recognition* **45**, 563–569 (2012).
35. Anstreicher, K. M. Recent advances in the solution of quadratic assignment problems. *Mathematical Programming* **97**, 27–42 (2003).
36. McAuley, J. J., Caetano, T. S. & Barbosa, M. S. Graph rigidity, cyclic belief propagation, and point pattern matching. *IEEE Transactions on Pattern Analysis and Machine Intelligence* **30**, 2047–2054 (2008).
37. Caetano, T. S., Caelli, T., Schuurmans, D. & Barone, D. A. C. Graphical models and point pattern matching. *IEEE Transactions on Pattern Analysis and Machine Intelligence* **28**, 1646–1663 (2006).
38. Thain, D., Tannenbaum, T. & Livny, M. Distributed computing in practice: the condor experience. *Concurrency and computation: practice and experience* **17**, 323–356 (2005).
39. Sonka, M., Hlavac, V. & Boyle, R. Image processing, analysis, and machine vision (2014).
40. Comin, M., Guerra, C. & Dellaert, F. Binding balls: Fast detection of binding sites using a property of spherical fourier transform. *Journal of Computational Biology* **16**, 1577–1591 (2009).
41. Padhorny, D. *et al.* Protein–protein docking by fast generalized fourier transforms on 5d rotational manifolds. *Proceedings of the National Academy of Sciences* **113**, E4286–E4293 (2016).
42. Sutton, A. P. & Balluffi, R. W. *Interfaces in crystalline materials* (Clarendon Press, 1995).

43. Patala, S., Mason, J. K. & Schuh, C. A. Improved representations of misorientation information for grain boundary science and engineering. *Progress in Materials Science* **57**, 1383–1425 (2012).
44. Patala, S. & Schuh, C. A. Symmetries in the representation of grain boundary-plane distributions. *Philosophical Magazine* **93**, 524–573 (2013).
45. Homer, E. R., Patala, S. & Priedeman, J. L. Grain boundary plane orientation fundamental zones and structure-property relationships. *Scientific reports* **5** (2015).
46. Bishop, G. H. & Chalmers, B. A coincidence-ledge-dislocation description of grain boundaries. *Scripta Metallurgica* **2**, 133–139 (1968).
47. Sutton, A. & Vitek, V. On the structure of tilt grain boundaries in cubic metals i. symmetrical tilt boundaries. *Philosophical Transactions of the Royal Society of London. Series A, Mathematical and Physical Sciences* **309**, 1–36 (1983).
48. Sutton, A. & Vitek, V. On the structure of tilt grain boundaries in cubic metals ii. asymmetrical tilt boundaries. *Philosophical Transactions of the Royal Society of London. Series A, Mathematical and Physical Sciences* **309**, 37–54 (1983).
49. Han, J., Vitek, V. & Srolovitz, D. J. The grain-boundary structural unit model redux. *Acta Materialia* **133**, 186–199 (2017).
50. Edge-contracted icosahedron. Edge-contracted icosahedron — Wikipedia, the free encyclopedia (2017). URL https://en.wikipedia.org/wiki/Edge-contracted_icosahedron. [Online; This page was last edited on 7 June 2017, at 16:12 (UTC).].
51. Han, J., Thomas, S. L. & Srolovitz, D. J. Grain-boundary kinetics: A unified approach. *arXiv preprint arXiv:1803.03214* (2018).
52. Balluffi, R. & Brokman, A. Simple structural unit model for core-dependent properties of symmetrical tilt boundaries. Tech. Rep. 8 (1983).
53. Balluffi, R. & Sutton, A. Why should we be interested in the atomic structure of interfaces? In *Materials Science Forum*, vol. 207, 1–12 (Trans Tech Publ, 1996).
54. Laws, K., Miracle, D. & Ferry, M. A predictive structural model for bulk metallic glasses. *Nature communications* **6** (2015).
55. Sheng, H., Luo, W., Alamgir, F., Bai, J. & Ma, E. Atomic packing and short-to-medium-range order in metallic glasses. *Nature* **439**, 419 (2006).
56. Ding, J., Cheng, Y.-Q., Sheng, H. & Ma, E. Short-range structural signature of excess specific heat and fragility of metallic-glass-forming supercooled liquids. *Physical Review B* **85**, 060201 (2012).
57. Cheng, Y.-Q. & Ma, E. Atomic-level structure and structure–property relationship in metallic glasses. *Progress in Materials Science* **56**, 379–473 (2011).
58. Cheng, Y. Q., Ma, E. & Sheng, H. W. Atomic level structure in multicomponent bulk metallic glass. *Physical Review Letters* **102**, 245501 (2009).
59. Plimpton, S. Fast parallel algorithms for short-range molecular dynamics. *Journal of Computational Physics* **117**, 1–19 (1995).
60. Wang, Q., Li, J. H., Liu, J. B. & Liu, B. X. Atomistic study of chemical effect on local structure in mg-based metallic glasses. *RSC Advances* **5**, 46861–46868 (2015).
61. Sun, Y. *et al.* ‘crystal genes’ in metallic liquids and glasses. *Scientific Reports* **6**, 23734 (2016).
62. Wang, S. Y. *et al.* Short- and medium-range order in a z73pt27 glass: Experimental and simulation studies. *Physical Review B* **78**, 184204 (2008).

63. Guo, G., Yang, L. & Wu, S. Structural investigation upon the high glass-forming ability in fe-doped zrcual multicomponent alloys. *Intermetallics* **71**, 24–30 (2016).
64. Peng, H. L., Li, M. Z. & Wang, W. H. Structural signature of plastic deformation in metallic glasses. *Physical Review Letters* **106**, 135503 (2011).
65. Cheng, Y. Q., Sheng, H. W. & Ma, E. Relationship between structure, dynamics, and mechanical properties in metallic glass-forming alloys. *Physical Review B* **78**, 014207 (2008).
66. Jakse, N. & Pasturel, A. Glass forming ability and short-range order in a binary bulk metallic glass by ab initio molecular dynamics. *Applied Physics Letters* **93**, 113104 (2008).
67. Patala, S. Approximating coincidence–turning a new page for bicrystallography. *Acta Crystallographica Section A: Foundations and Advances* **73**, 85–86 (2017).
68. Zhang, W.-Z., Sun, Z.-P., Zhang, J.-Y., Shi, Z.-Z. & Shi, H. A near row matching approach to prediction of multiple precipitation crystallography of compound precipitates and its application to a mg/mg 2 sn system. *Journal of Materials Science* **52**, 4253–4264 (2017).
69. Gaskell, P. H. A new structural model for amorphous transition metal silicides, borides, phosphides and carbides. *Journal of Non-Crystalline Solids* **32**, 207–224 (1979).
70. Wales, D. J., Doye, J. P., Miller, M. A., Mortenson, P. N. & Walsh, T. R. Energy landscapes: from clusters to biomolecules. *Advances in Chemical Physics, Volume 115* 1–111 (2007).
71. Ferrando, R., Jellinek, J. & Johnston, R. L. Nanoalloys: from theory to applications of alloy clusters and nanoparticles. *Chemical reviews* **108**, 845–910 (2008).
72. Schön, J. & Jansen, M. Determination, prediction, and understanding of structures, using the energy landscapes of chemical systems–part i. *Zeitschrift für Kristallographie-Crystalline Materials* **216**, 307–325 (2001).
73. Schön, J. & Jansen, M. Determination, prediction, and understanding of structures, using the energy landscapes of chemical systems–part ii. *Zeitschrift für Kristallographie/International journal for structural, physical, and chemical aspects of crystalline materials* **216**, 361–383 (2001).
74. Yang, J., Li, H., Campbell, D. & Jia, Y. Go-icp: A globally optimal solution to 3d icp point-set registration. *IEEE Transactions on Pattern Analysis and Machine Intelligence* **38**, 2241–2254 (2016). DOI 10.1109/TPAMI.2015.2513405.

Supplemental Materials:

Point-Pattern Matching Technique for Local Structural Analysis in Condensed Matter

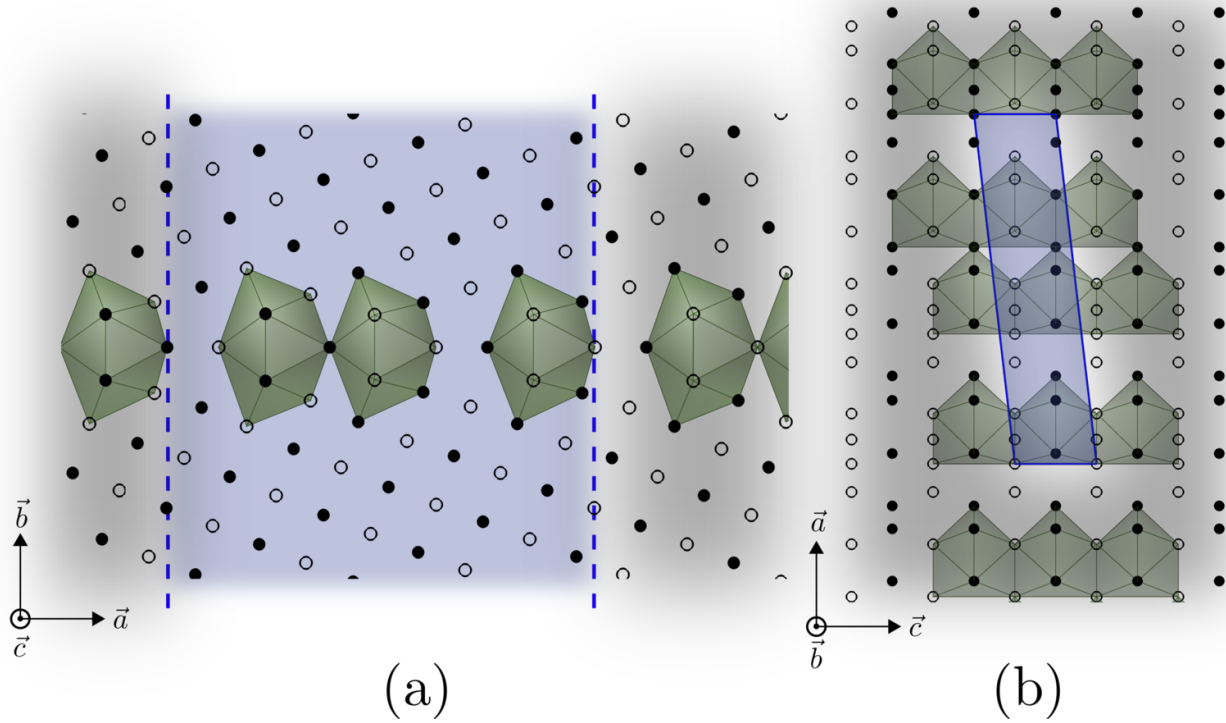


Figure S1. The atomistic structure of $\Sigma 73$ ($0\bar{3}8$) GB is shown. The views in (a) and (b) are along the tilt axis and boundary-plane normal, respectively. The axes in the figure, \vec{a} , \vec{b} and \vec{c} correspond to the $[083]$, $[0\bar{3}8]$ and $[100]$ lattice directions, respectively.

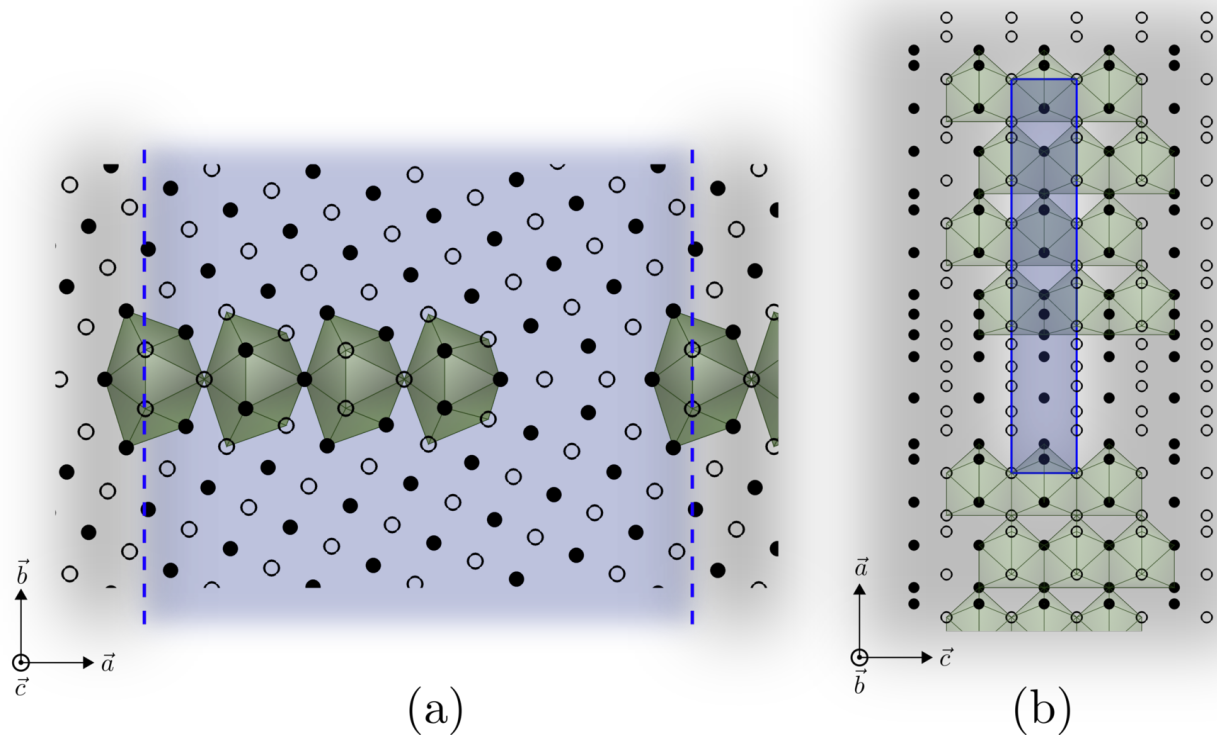
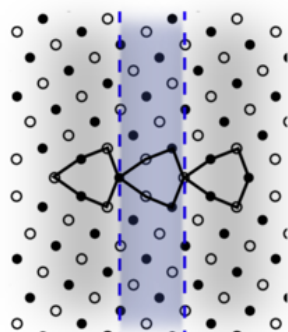
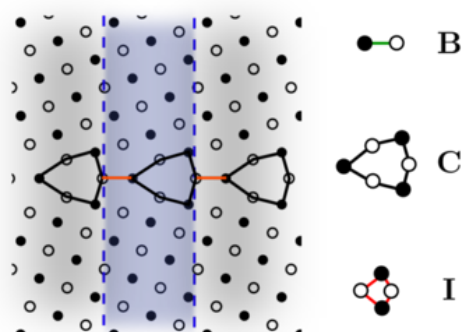


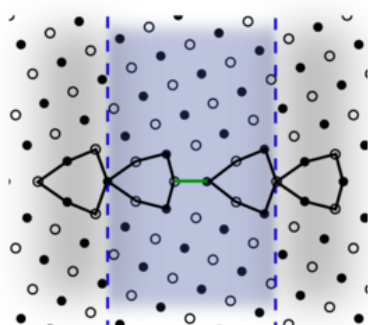
Figure S2. The atomistic structure of $\Sigma 73$ $(0 \bar{1} 1 5)$ GB is shown. The views in (a) and (b) are along the tilt axis and boundary-plane normal, respectively. The axes in the figure are such that, $\vec{a} = [0 \bar{5} \bar{1} 1]$, $\vec{b} = [0 \bar{1} 1 5]$ and $\vec{c} = [\bar{1} 0 0]$.



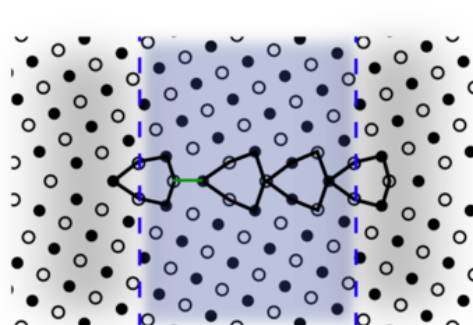
(a) $\Sigma 5 (0 \bar{1} 3)$



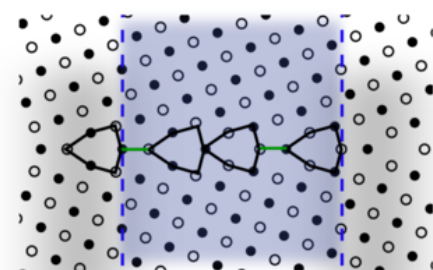
(b) $\Sigma 5 (0 \bar{2} 1)$



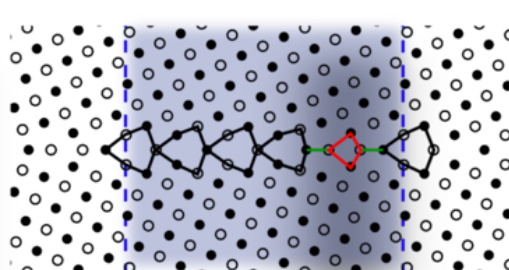
(c) $\Sigma 29 (0 \bar{2} 5)$



(d) $\Sigma 29 (0 \bar{7} 3)$



(e) $\Sigma 73 (0 \bar{3} 8)$



(f) $\Sigma 73 (0 \bar{11} 5)$

Figure S3. The Structural Unit Model representations of all the GBs analyzed in this article are shown.